Satellite Hyperspectral Imaging Simulation

Slawomir Blonski, Changyong Cao, Jerry Gasser, Robert Ryan
Lockheed Martin Space Operations, Stennis Programs
Stennis Space Center, Mississippi

Vicki Zanoni, Tom Stanley
NASA Commercial Remote Sensing Program
Stennis Space Center, Mississippi

Satellite Hyperspectral Imaging Simulation*

Slawomir Blonski, Changyong Cao, Jerry Gasser, Robert Ryan
Lockheed Martin Space Operations, Stennis Programs
Stennis Space Center, Mississippi

Vicki Zanoni, Tom Stanley
NASA Commercial Remote Sensing Program
Stennis Space Center, Mississippi

ABSTRACT

Simulations of generic pushbroom satellite hyperspectral sensors have been performed to evaluate the potential performance and validation techniques for satellite systems such as COIS (NEMO), Warfighter-1 (OrbView-4), and Hyperion (EO-1). The simulations start with a generation of synthetic scenes from material maps of studied terrain. Scene- reflected radiance is corrected for atmospheric effects and convolved with sensor spectral response using MODTRAN 4 radiance and transmission calculations. Scene images are further convolved with point spread functions derived from Optical Transfer Functions (OTF's) of the sensor system. Photon noise and detector/electronics noise are added to the simulated images, which are also finally quantized to the sensor bit resolution. Studied scenes include bridges and straight roads used for evaluation of sensor spatial resolution, as well as fields of minerals, vegetation, and manmade materials used for evaluation of sensor radiometric response and sensitivity. The scenes are simulated with various seasons and weather conditions. Signal-to-noise ratios and expected performance are estimated for typical satellite system specifications and are discussed for all the scenes.

Key words: hyperspectral remote sensing, sensor design, computer simulations, virtual prototyping

I. INTRODUCTION

Hyperspectral imaging is an exciting, emerging, remote sensing technology that enables one instrument to have utility for a wide range of applications. Because hyperspectral sensors record hundreds of spectral bands for each location they image, the data they provide significantly improve capabilities for automated atmospheric correction, spectral unmixing, and feature extraction, which form the basis for many remote sensing applications. In the near future, three satellites with hyperspectral sensors are going to be launched into low earth orbits. The instruments include the Coastal Ocean Imaging Spectrometer (COIS) on the Naval EarthMap Observer (NEMO) satellite, Warfighter-1 on the OrbView-4 commercial satellite, and Hyperion on the NASA's Earth Observing-1 (EO-1) spacecraft. Despite some distinct differences between the instruments, their ability to provide hyperspectral image cubes from space-borne platforms is the common feature which encourages comparison and cross-validation between them. AVIRIS, an airborne hyperspectral sensor used on the ER-2 and Twin Otter platforms, is a demonstration of the outstanding radiometric performance, which can be achieved by such a system (Green et al. 1998). To understand what kind of performance one can expect from the satellite hyperspectral sensors, we have created a computational prototype of a generic hyperspectral sensor on a satellite platform. In recent years, rapid advances in computer technology have allowed computational modeling and simulations to become valuable tools in predicting performance characteristics of future instruments and devices before physical parts are made and assembled (Blonski et al. 1997). The Virtual Product Laboratory (VPL) software environment developed at the NASA Stennis Space Center allows for such studies of remote sensing systems (Gasser et al. 1999).

II. INSTRUMENT DESIGN

Our virtual hyperspectral instrument is a pushbroom system with a reflective telescope, a prism spectrograph, and a state-of-the-art focal plane array detector optimized for the visible and SWIR spectral regions. The sensor is designed to provide imagery with a 30-m ground sampling distance (GSD) from the altitude of 705 km. Because the focal plane array is supposed to have detector pitch of 24 μm (with 100% fill factor), the required effective focal length

* Paper prepared for submittal to the 1999 International Symposium on Spectral Sensing Research. This work was supported by the NASA Commercial Remote Sensing Program Office, under contract number NAS 13-650 at the John C. Stennis Space Center, Mississippi.

of the optics is 564 mm. Therefore, the instantaneous field of view (IFOV), defined here as a sampling interval, not as the full width at half maximum (FWHM) of a point-spread function, is 0.0426 mrad. Additionally, because we also assume that the detector array has 640 pixels in the spatial (cross-track) direction, field of view of the sensor is 1.5°. A reflective telescope with the Cassegrain design and f/3 is the most appropriate for such a case (Smith 1992). This f/# implies aperture size of 188 mm. Optical efficiency of the combined telescope - spectrograph system is conservatively assumed to be 10% over the entire spectral range. The optics are supposed to be only diffraction-limited, with no aberration blur. Spectral range of the sensor is from 400 nm to 2500 nm, with the sampling interval of 10 nm – 211 bands with the Gaussian shape and FWHM of 10 nm. The detector array and electronics are also characterized by an integration time of 4 ms and a 12-bit quantization. A simple noise model, which accounts for the detector and electronics noise (the illumination-independent noise floor) as well as the photon (shot) noise, is applied in the simulations. The noise floor is assumed to be 5 nW / (cm^2 sr nm). The satellite is additionally supposed to introduce random jitter with an RMS blur of 0.0242 mrad. Although without much detailed knowledge of a specific design, and without simulations on a sub-system level, it is difficult to estimate the actual performance parameters such as the optical efficiency or the noise floor, we have selected values, which we believe would be typical for present-day hyperspectral sensor systems. Table I lists the parameters of the simulated sensor.

Table I. Characteristics of the simulated satellite hyperspectral sensor system

Altitude	705 km
GSD	30 m
Spectral range	400 - 2500 nm
Spectral sampling	10 nm
Spectral resolution	10 nm
Number of spectral bands	211
Spatial sampling (IFOV)	0.0426 mrad
Field of view	1.5°
Detector pitch	24 μm
Effective focal length	564 mm
F/#	3
Aperture diameter	188 mm
Optical efficiency	10%
Integration time	4 ms
Quantization	12 bits
Noise floor	5 nW / (cm^2 sr nm)
Random jitter RMS blur	0.0242 mrad

III. SENSOR MODEL

A system level approach based on Optical Transfer Functions (OTF's) is applied in the modeling of the sensor (Kopeika 1998). System OTF is formed by multiplication of individual functions taking into account the following factors:

- Detector size
- Diffraction
- Linear motion
- Random jitter
- Atmospheric turbulence

The system OTF is assumed to be separable in two orthogonal axes coincident with the detector array axes, one of which is parallel (and the other is perpendicular) to the direction of the satellite ground track. In both cross-track and along-track directions, the individual OTF's are described by formulae presented below. Using detectors of finite size to spatially sample a scene results in the detector OTF is given by the equation (Holst 1998):

$$\mathrm{OTF}_{\mathrm{detector}}(u) = \mathrm{sinc}(\pi u d / f)$$

where u is the object-space spatial frequency, d is the detector size, and f is the effective focal length of the optics. The sinc function is defined here by:

$$\mathrm{sinc}(x) = \begin{cases} 1 & x = 0 \\ \dfrac{\sin x}{x} & x \neq 0 \end{cases}$$

Diffraction in the optical system results in image blurring described by the following function (Holst 1998):

$$\mathrm{OTF}_{\mathrm{diffraction}}(u) = \begin{cases} \dfrac{2}{\pi}\left[\cos^{-1}(u/u_0) - (u/u_0)\sqrt{1-(u/u_0)^2}\right] & u \leq u_0 \\ 0 & u > u_0 \end{cases}$$

with $u_0 = D / \lambda$, where D is the aperture size and λ is the wavelength. OTF associated with the orbital motion of the satellite is given by (Holst 1998, Kopeika 1998):

$$\mathrm{OTF}_{\mathrm{motion}}(u) = \mathrm{sinc}(\pi u v \tau / h)$$

where h is the altitude of the satellite above the earth's surface, v is the speed of the subsatellite point on the ground, and τ is the integration time. The motion OTF affects the system OTF only in the

along-track direction. The random jitter OTF is approximated with a Gaussian function (Holst 1998):

$$\mathrm{OTF}_{\mathrm{jitter}}(u) = \exp(-2\pi^2 b^2 u^2)$$

where b is an object-space RMS diameter of the blur created by the random motion. The expression for the atmospheric turbulence OTF is based on the Fried's approach (Fried 1966, Beland 1993):

$$\mathrm{OTF}_{\mathrm{turbulence}}(u) = \exp\left\{-\left[\tfrac{24}{5}\Gamma(\tfrac{6}{5})\right]^{5/6}(\lambda u / r_0)^{5/3}\left[1-\kappa(\lambda u / D)^{1/3}\right]\right\}$$

where r_0 is called the atmospheric coherence length or the Fried's seeing parameter, Γ is the Gamma function, and the factor κ is specified in the following way:

- $\kappa = 0$ for long exposure times ($\tau \geq 10$ ms)
- $\kappa = 0.5$ for short exposure times ($\tau < 10$ ms) and far-field propagation ($h \geq D^2/\lambda$)
- $\kappa = 1$ for short exposure times ($\tau < 10$ ms) and near-field propagation ($h < D^2/\lambda$)

Note: $\left[\tfrac{24}{5}\Gamma(\tfrac{6}{5})\right]^{5/6} \approx 3.44$. In this study, a value of 20 cm, which is better than a typical one, is assumed for the Fried's parameter (Beland 1993).

Figures 1 and 2 show absolute values of OTF's calculated for the simulated sensor.

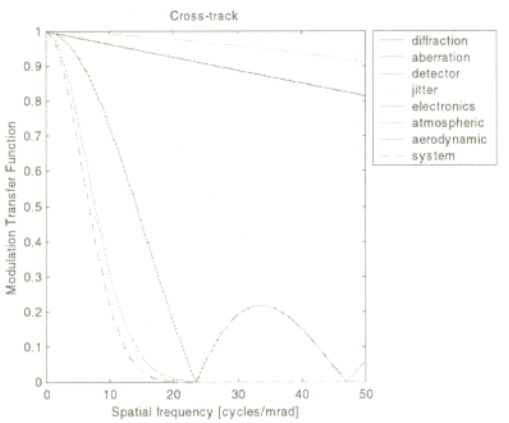

Figure 1. Cross-track modulation transfer function of the simulated sensor for band 16 (550 nm).

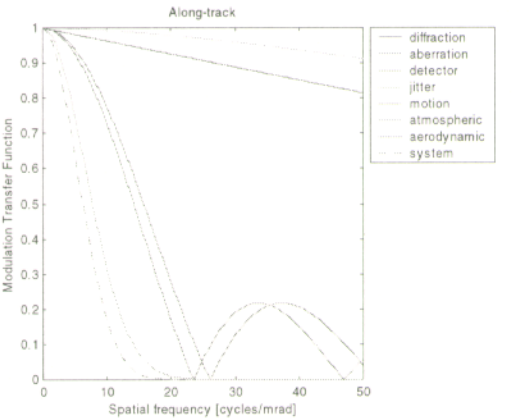

Figure 2. Along-track modulation transfer function of the simulated sensor for band 16 (550 nm).

IV. IMAGING SIMULATION

Both cross-track and along-track components of the system OTF are used to derive a point spread function (PSF) for the sensor using an inverse Fourier transform. The calculations are performed in a discrete fashion using the fast Fourier transform (FFT) algorithm and a series of spatial frequencies dependent on ground sampling distance with which an input scene is defined. Range of the PSF is truncated to a rectangular area where the cross-track and along-track components of PSF are no less then 1% of their maximum values. To protect radiometric accuracy of the simulations, the truncated PSF is normalized in such a way that a sum of all the elements of the PSF matrix is equal to one. The input scene image is convolved with the PSF to generate an image created by the simulated sensor. The convolution is performed in the spatial domain because we found that this approach offers better performance than the one based on two-dimensional FFT. The savings are created when the convolution is performed as a block operation with the PSF kernel moving over the scene image with step defined by the sensor sampling distance. To ensure quality of the simulations, the input scene must be created with spatial sampling significantly finer than that of the sensor. Recent studies have shown that simulations with the sampling ratios of 3 to 7 produce adequate results (Jacobs & Edwards 1999). However, only sampling in the direction perpendicular to an edge was considered in that work. Our tests have indicated that much larger oversampling is needed to reliably simulate images of edges oblique to the sampling direction. Therefore, an oversampling of 15 was used in the present simulations. However, one must realize

that such an oversampling comes with a significant computational price, especially in the amount of disk space required to store the scene image cubes. There is definitely a need for further studies on how to achieve the desired fidelity of the simulations while keeping the computational requirements in check.

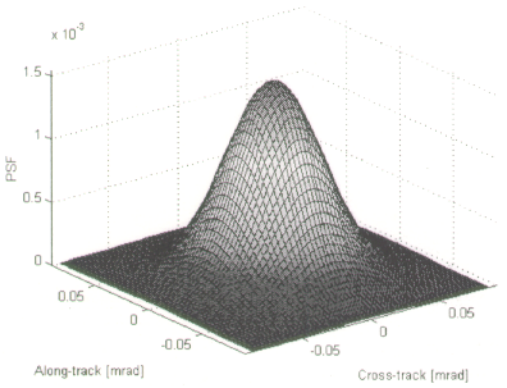

Figure 3. Point spread function of the simulated sensor for band 16 (550 nm). The mesh is drawn using the sampling interval of an input scene.

After the image convolution, detector and electronics noise as well as photon noise is added to each pixel of the simulated image. To simulate the photon noise, first the pixel radiance L is converted into the number of photons n using the following formula:

$$n = \varepsilon \frac{\delta^2}{g_{\max}} \frac{\pi D^2}{4H^2} \Delta\lambda \frac{\tau\lambda_0}{hc} L$$

where:

ε	optical efficiency
δ	spatial sampling interval of an input scene
$g_{\max}$	maximum value of the PSF
D	sensor aperture diameter
H	satellite altitude
$\Delta\lambda$	spectral band width
λ_0	spectral band center wavelength
τ	integration time
h	Planck's constant
c	speed of light

Then, a random number, which is generated according to the Poisson distribution with the mean value equal to the number of photons, replaces the original value. For large numbers of photons, the Poisson distribution is approximated by the normal distribution with the mean value equal to the number of photons and the standard deviation equal to the square root of the number of photons. Finally, the number of photons is converted back into radiance by reversing the above formula. Next, adding a random number generated according to the normal distribution with standard deviation equal to the noise floor simulates the detector and electronics noise. Intensity of the simulated image is additionally quantized to the number of levels given by the number of bits provided by the sensor for each pixel. The OTF and PSF calculations, the convolution, and the noise simulations are performed separately for each spectral band of the sensor, but at the end the output images are combined into an image cube.

V. SYNTHETIC SCENE

While the scene radiance is convolved with the sensor *spatial* response during the imaging simulation phase, its convolution with the sensor *spectral* response is done during creation of the synthetic scene. In general, the simulation process (without effects of noise) can be summarized in the following formula (Schowengerdt 1997):

$$I(x_0, y_0, \lambda_0) = \iiint L(x, y, \lambda) R(\lambda - \lambda_0) PSF(x - x_0, y - y_0, \lambda) dx dy d\lambda$$

where I is the simulated sensor-generated image, L is the synthetic scene spectral radiance, R is the sensor spectral response, and PSF is the sensor spatial response (the point spread function). Assuming that the PSF does not change significantly for the wavelengths within a single spectral band, the spatial convolution can be separated from the spectral convolution to result in:

$$I(x_0, y_0, \lambda_0) = \iint \overline{L}(x, y, \lambda_0) PSF(x - x_0, y - y_0, \lambda_0) dx dy$$

where the in-band radiance is given by:

$$\overline{L}(x, y, \lambda_0) = \int L(x, y, \lambda) R(\lambda - \lambda_0) d\lambda$$

Although, in our implementation, it is done in a discrete fashion, nevertheless, the former integral is calculated during the imaging simulations, while the latter is evaluated during atmospheric radiative transfer calculations of the synthetic scene creation process. These calculations also incorporate into the simulations the geometric properties of the satellite motion: altitude above the Earth's surface and azimuth of the ground track as well as orientation of the line-of-sight.

Image cubes of the synthetic scenes used as input for the simulations can be generated in one of the following three ways. The first approach uses the DIRSIG software package developed at Rochester Institute of Technology (Schott et al. 1999). DIRSIG uses facetized models of terrain and objects such as buildings or vehicles to calculate scene radiance by performing ray tracing and atmospheric radiative transfer modeling based on MODTRAN. The second option is to use GCI Toolkit, which is a commercial software package developed by Photon Research Associates. GCI Toolkit uses rasterized models of terrain and clouds as well as atmospheric modeling based on MOSART. Availability of the rasterized terrain databases with sufficiently high spatial resolution limits our ability to use GCI Toolkit in the current simulations. The third approach is an *ad hoc* combination of a two-dimensional material map and the atmospheric radiative transfer model of MODTRAN. Such calculations are described in detail in another paper in these proceedings (Cao et al. 1999).

For the signal-to-noise ratio (S/N) studies presented in this paper, flat uniform scenes, with the same material defined for all the pixels, were created using the third method. MODTRAN 4 was executed using the correlated-k option (Berk et al. 1998) for the geographic location of the scene in the proximity of New Orleans, Louisiana, at 30° N latitude and 90° W longitude. Because of the location, the mid-latitude summer model atmosphere was assumed for all the seasons, and as a result the only difference between the seasons is in the Earth to sun distance and the sun's location in the sky. These differences are introduced by performing the calculations for the day of the year number 80 (spring), 172 (summer), and 356 (winter). Other parameters included: CO_2 mixing ratio of 360 ppm_v, water column scaling factor of 0.5, the default vertical ozone column, rural visibility of 23 km, and a nadir looking from the top of atmosphere. Reflectance spectra of surfaces used in the simulations were obtained from the ASTER Spectral Library (version 1.1), which includes data from three sources: the Johns Hopkins University (JHU) Spectral Library, the Jet Propulsion Laboratory (JPL) Spectral Library, and the United States Geological Survey (USGS - Reston) Spectral Library (for reference, see the WWW page at URL http://speclib.jpl.nasa.gov).

VI. RESULTS

The synthetic scene of the Rochester area was used to test capabilities of the hyperspectral imaging simulations.

Figure 4. Image of a synthetic scene created using DIRSIG with 1 m GSD and the 211 spectral bands of the simulated sensor. Bands 23 (620 nm), 16 (550 nm), and 7 (460 nm) are displayed as the RGB colors, respectively. Prof. John Schott, Rochester Institute of Technology, provided the model geometry for this scene based on the Genesee River Gorge area in Rochester, New York.

An image cube of the input scene consisted of 1024 by 1024 pixels and 211 bands. Simulations of the imaging process do not change the number of spectral bands, while reducing the spatial resolution (see Figure 5). Effects of spatial sampling as well as optics and atmosphere are clearly visible when the simulated image (Figure 6) is compared with an image of the input scene (Figure 4).

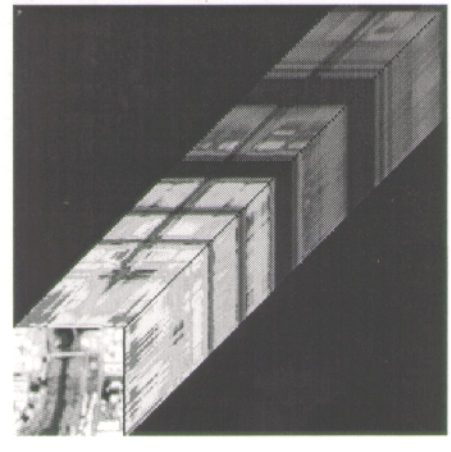

Figure 5. Image cube generated by the simulated hyperspectral sensor from the synthetic scene of the Rochester area created with DIRSIG.

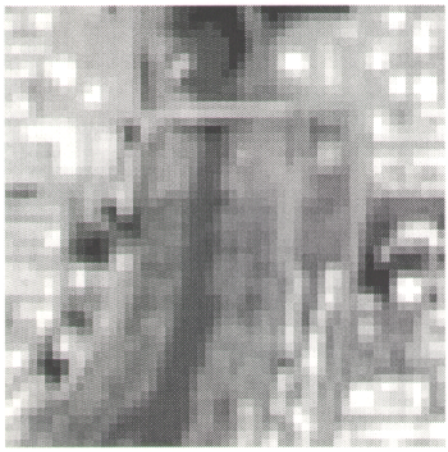

Figure 6. Image generated by the simulated sensor from the synthetic scene of the Rochester area created with DIRSIG. Bands 23 (620 nm), 16 (550 nm), and 7 (460 nm) are displayed as the RGB colors, respectively.

Image cubes created in the simulations performed with the uniform scenes for the S/N studies consisted of 100 by 100 pixels and 211 bands. For each of the bands, mean and standard deviation of image intensity were calculated using all the 10,000 pixels. The mean divided by the standard deviation was used as an estimate of the signal-to-noise ratio for the material used in the given uniform scene. Surfaces of the following materials were used in the studies:

- water
- minerals:
  alunite, calcite, dolomite, kaolinite, quartz
- soils:
  black loam, brown loam, dark loam, dune sand, gray clay
- vegetation:
  dry long grass, lawn grass, sage brush, fir tree, pine tree
- man-made materials:
  aluminum, asphalt, concrete, steel, terra cotta

For each material, three scenes were created with atmospheric effects calculated using solar conditions for different seasons: winter, spring, and summer. Spectral radiance and noise equivalent spectral radiance (NESR) obtained in the simulations with the water surface are shown in Figure 7 and Figure 8, respectively. Because of the low reflectance of the water surface, the signal-to-noise ratios shown in Figure 9 are relatively low. In the visible region, the NESR is dominated by the photon noise, while the detector and electronics noise are prevalent in SWIR. Although we have assumed that optical efficiency and noise floor of the simulated sensor are independent of the radiation wavelength, this illustrates effects of spectral properties of solar illumination on signal-to-noise ratios in hyperspectral remote sensing imagery. Future simulations, conducted also on a subsystem level to include the wavelength dependence, may provide more insights into this problem.

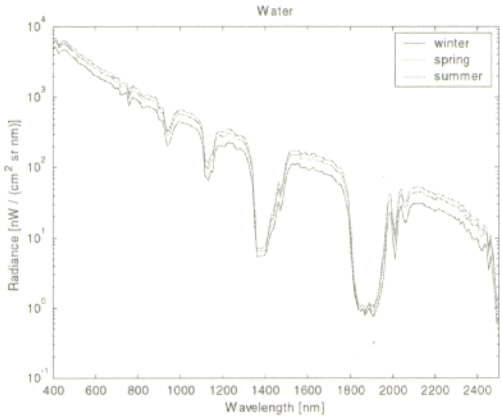

Figure 7. Spectral radiance measured by the simulated satellite sensor for water.

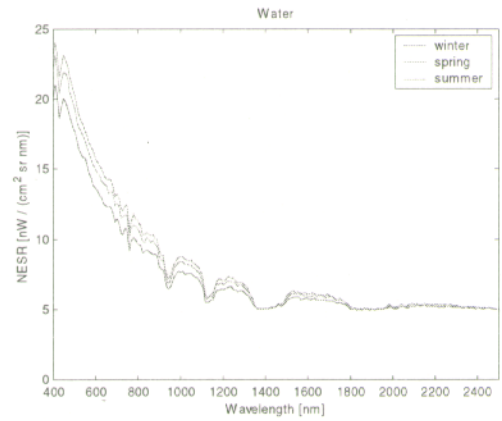

Figure 8. NESR obtained for the simulated satellite sensor observing a water surface.

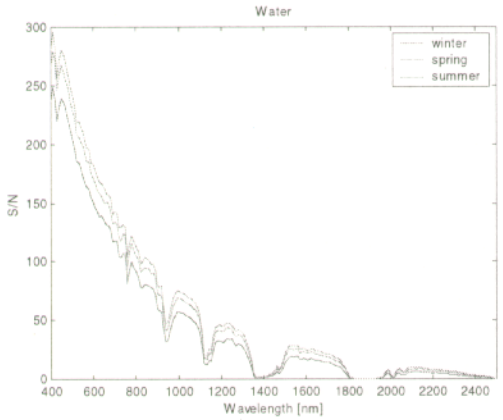

Figure 9. S/N obtained for the simulated satellite sensor observing a water surface.

Mineral surfaces provide much higher signal-to-noise ratios than water. These are the highest S/N values among all the studied materials. S/N for calcite is shown as an example in Figure 10, but for all the studied minerals the values are similar. S/N for dune sand is similar to that of minerals (see Figure 11). Other soils display substantially lower S/N, as shown in Figure 12 for gray clay as a typical example. Surface of concrete offers S/N, which is similar to that of soils, although it is slightly better in the visible region. Chlorophyll edge is clearly displayed in the S/N spectrum obtained with pine trees and shown in Figure 14, which is typical for almost all the vegetation, with exception of the dry long grass also studied in this group. For the man-made materials such as asphalt (Figure 15) and steel (Figure 16) as well as aluminum and terra cotta, S/N is also influenced by the characteristic reflectance spectra of the surfaces.

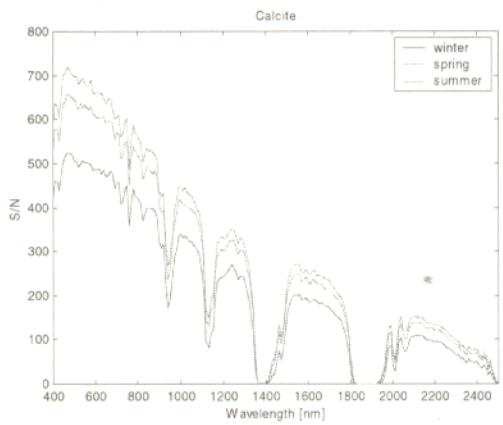

Figure 10. Signal-to-noise ratios obtained for the simulated satellite sensor observing calcite.

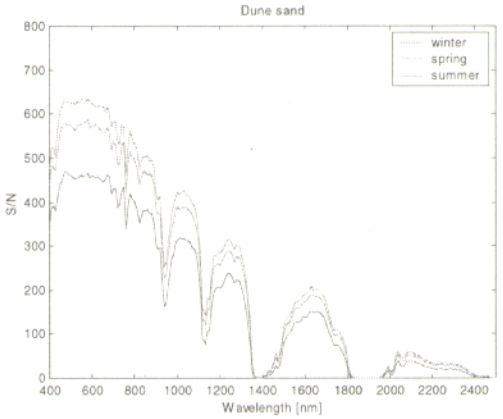

Figure 11. Signal-to-noise ratios obtained for the simulated satellite sensor observing dune sand.

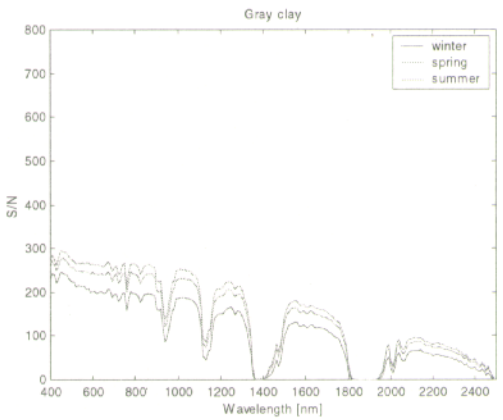

Figure 12. Signal-to-noise ratios obtained for the simulated satellite sensor observing gray clay.

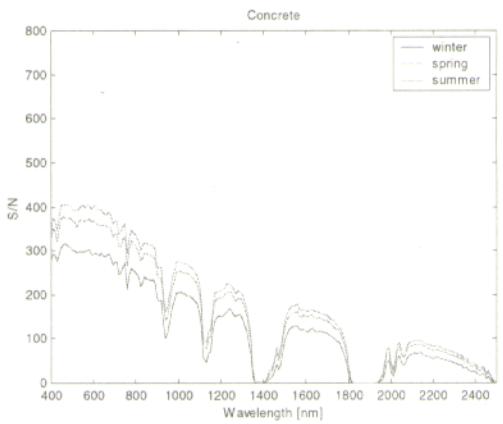

Figure 13. Signal-to-noise ratios obtained for the simulated satellite sensor observing concrete.

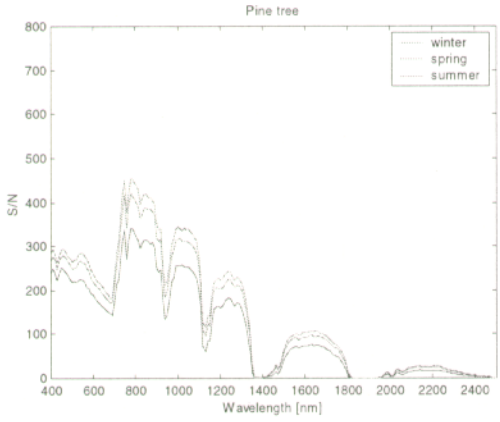

Figure 14. Signal-to-noise ratios obtained for the simulated satellite sensor observing pine trees.

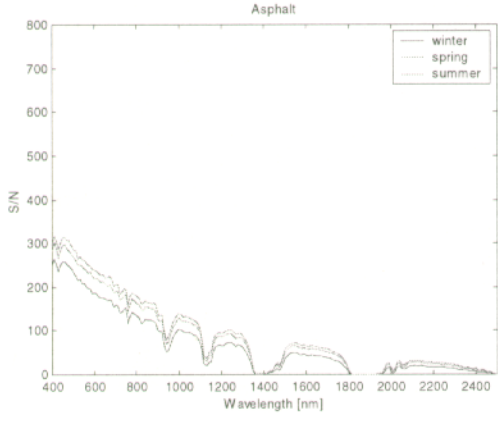

Figure 15. Signal-to-noise ratios obtained for the simulated satellite sensor observing asphalt.

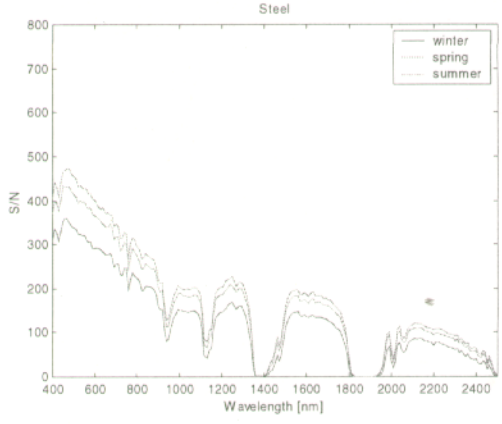

Figure 16. Signal-to-noise ratios obtained for the simulated satellite sensor observing steel.

VII. CONCLUSIONS

We have described physics-based, end-to-end simulations of a remote sensing satellite system, which includes a hyperspectral electro-optical sensor working in the visible and SWIR spectral regions. The simulations start with modeling of the Earth's surface: creation of a synthetic scene with spectral radiance provided for each of its elements. That process also includes modeling of radiance propagation through the atmosphere. In the next step, the at-sensor radiance is transformed using sensor effects defined by spatial sampling, optical transfer functions, and noise model. The calculations are performed for each spectral band of the sensor, so at the end, an image cube generated by the simulated sensor is created. The simulated image cubes are further analyzed according to a planned application, such as the signal-to-noise studies presented in this paper. These studies have shown that a hyperspectral satellite sensor can provide reasonable signal-to-noise ratios for minerals, soils, vegetation, and man-made materials, while values of S/N are crucial in accurate spectral unmixing and classification of remote sensing data.

VIII. REFERENCES

Beland, R.R., in: Atmospheric Propagation of Radiation, Smith, F.G., ed., ERIM / SPIE Press, 1993, pp. 157-232.

Berk, A., Bernstein, L.S., Anderson, G.P., Acharya, P.K., Robertson, D.C., Chetwynd, J.H., Adler-Golden, S.M., "MODTRAN Cloud and Multiple Scattering Upgrades with Application to AVIRIS," Remote Sensing of Environment, Vol. 65, No. 3, 1998, pp. 367-375.

Blonski, S., Lean, M.H., Jensen, J.L., Crosier, R.B., Schlein, M.S., "Computational Prototyping of the Chemical Imaging Sensor," Proceedings of SPIE, Vol. 3118, 1997, pp. 330-338.

Cao, C., Blonski, S., Ryan, R., Gasser, J., Zanoni, V., Jenner, J., "Synthetic Scene Generation of the Stennis V&V Target Range for the Calibration of Remote Sensing Systems," Proceedings of the International Symposium on Spectral Sensing Research, Las Vegas, Nevada, 1999.

Fried, D.L., "Optical Resolution Through a Randomly Inhomogeneous Medium for Very Long and Very Short Exposures," Journal of the Optical Society of America, Vol. 56, No. 10, 1966, pp. 1372-1379.

Gasser, J., Cao, C., Blonski, S., McConnell, K., Ryan, R., Zanoni, V. "NASA's Virtual Product Laboratory Overview," Proceedings of the International Symposium on Spectral Sensing Research, Las Vegas, Nevada, 1999.

Green, R.O., Pavri, B., Faust, J., Williams, O., Chovit, C., "Inflight Validation of AVIRIS Calibration in 1996 and 1997," Proceedings of the AVIRIS Airborne Geoscience Workshop, Pasadena, California, 1998.

Holst, G.C., CCD Arrays, Cameras, and Displays, Second edition, JCD/SPIE Press, 1998.

Jacobs, E.L., Edwards, T.C., "Sampling Criteria for Sensor Simulation," Optical Engineering, Vol. 38, No. 5, 1999, pp. 827-835.

Kopeika, N.S., A System Engineering Approach to Imaging, SPIE Press, 1998.

Schott, J.R., Brown, S.D., Raqueno, R.V., Gross, H.N., Robinson, G., "Advanced synthetic image generation models and their application to multi/hyperspectral algorithm development," Proceedings of SPIE, Vol. 3584, 1999, pp. 211-220.

Schowengerdt, R.A., Remote Sensing, Models and Methods for Image Processing, Second edition, Academic Press, 1997.

Smith, W.J., Modern Lens Design, McGraw Hill, 1992, p. 20.

REPORT DOCUMENTATION PAGE

Form Approved
OMB No. 0704-0188

1. REPORT DATE *(DD-MM-YYYY)*	2. REPORT TYPE	3. DATES COVERED *(From - To)*
01-10-1999		

4. TITLE AND SUBTITLE
Satellite Hyperspesctral Imaging Simulation

5a. CONTRACT NUMBER
NAS13-650

5b. GRANT NUMBER

5c. PROGRAM ELEMENT NUMBER

6. AUTHOR(S)
Slawomir Blonski
Changyong Cao
Jerry Gasser
Robert Ryan
Vicki Zanoni
Tom Stanley

5d. PROJECT NUMBER

5e. TASK NUMBER

5f. WORK UNIT NUMBER

7. PERFORMING ORGANIZATION NAME(S) AND ADDRESS(ES)
Lockheed Martin Stennis Programs

8. PERFORMING ORGANIZATION REPORT NUMBER
SE-1999-09-00022-SSC

9. SPONSORING/MONITORING AGENCY NAME(S) AND ADDRESS(ES)
Earth Science Applications Directorate

10. SPONSORING/MONITOR'S ACRONYM(S)

11. SPONSORING/MONITORING REPORT NUMBER

12. DISTRIBUTION/AVAILABILITY STATEMENT
Publicly Available STI per form 1676

13. SUPPLEMENTARY NOTES
Conference - Internaitonal symposium on spectral Snesing Research

14. ABSTRACT

Simulations of generic pushbroom satellite hyperspectral sensors have been performed to evaluate the potential performance and validation techniques for satellite systems such as COIS(NEMO), Warfighter-1 (OrbView-4) and Hyperion (EO-1). The simulations start with a generation of synthetic scenses from material maps of studied terrain. Scene-reflected radiance is corrected for atmospheric effects and convolved with sensor spectral response using MODTRAN 4 radiance and transmissions calculations. Scene images are furhter convolved with point spread functions derived from Optical Transfer Functions (OTF's) of the sensor system. Photon noise and etectorr/electronics noise are added to the simulated images, which are also finally quantized to the sensor bit resolution. Studied scenes include bridges and straight roads used for evaluation of sensor spatial resolution, as well as fields of minerals, vegetation and manmade materials used for evaluation of sensor radiometric response and sensitivitiy. The scenes are simulated with various seasons and weather conditions. Signal-to-moise ratios and expected perfomrance are estimated for typical satellite system specifications and are discussed for all the scenes.

15. SUBJECT TERMS

16. SECURITY CLASSIFICATION OF:			17. LIMITATION OF ABSTRACT	18. NUMBER OF PAGES	19b. NAME OF RESPONSIBLE PERSON
a. REPORT	b. ABSTRACT	c. THIS PAGE			Slawomir Bolonski
					19b. TELEPHONE NUMBER *(Include area code)*
U	U	U	UU	5	(228) 688-1944